Snapshot Performance of the Dominant Mode Rejection Beamformer

Kathleen E. Wage, *Member, IEEE*, and John R. Buck, *Member, IEEE*

***Abstract*—The dominant mode rejection (DMR) beamformer constructs its weight vector using a structured covariance estimate derived from the eigendecomposition of the sample covariance matrix (SCM). Like all adaptive beamformers (ABFs), the DMR ABF places notches in the direction of loud interferers to facilitate the detection of quiet targets. This paper investigates how DMR performs as a function of the number of snapshots used to estimate the SCM. The analysis focuses on the fundamental case of a single interferer in white noise. Theoretical calculations for the ensemble case reveal the relationships among notch depth, white noise gain, and SINR. The centerpiece of the paper is a detailed empirical study of the single-interferer case, which includes snapshot-deficient scenarios often ignored in previous work. Empirical data demonstrate that the sample eigenvectors determine the mean performance of the DMR ABF. On a log–log plot the mean notch depth is a piecewise linear function of the number of snapshots and the interference-to-noise ratio. The paper interprets the behavior of the DMR ABF using recent results on sample eigenvectors derived from random matrix theory.**

***Index Terms*—Adaptive beamformer (ABF), dominant mode rejection (DMR), eigendecomposition, random matrix theory (RMT), sample covariance matrix (SCM).**

I. Introduction

ONE goal of passive sonar array processing is to remove loud interferers to detect and localize quiet sources. Conventional beamformers (CBFs) are typically unable to achieve this goal due to high levels of interference. When the CBF is steered toward a quiet source, loud interferers can leak through the high sidelobes of the conventional beampattern and mask the low-level source signal. Adaptive beamformers (ABFs) place notches in the direction of loud interferers, thereby facilitating the detection of quiet targets. The minimum variance distortionless response (MVDR) beamformer, also known as the Capon beamformer [1], is derived by minimizing output power subject to a unity gain constraint in the look direction. The MVDR weight vector is a function of the inverse of the noise covariance matrix and the replica vector in the look direction. Assuming the ensemble covariance matrix (ECM) is available and there are fewer interferers than sensors, the MVDR processor has deep notches in its beampattern corresponding to the locations of the loud interferers. When the MVDR ABF is steered toward a quiet source, the notches prevent loud interferers from leaking through the sidelobes, guaranteeing a higher signal-to-interference-and-noise ratio (SINR) for the signal of interest.

In most practical applications, ensemble statistics are not available, and beamformers must be implemented using sample statistics. Performance depends on the number of data snapshots used to estimate the sample covariance matrix (SCM). Reed *et al.* show that the MVDR ABF requires twice as many snapshots as sensors to achieve a mean output SINR within 3 dB of the SINR achievable with ensemble statistics [2]. Reed *et al.* assume that the desired signal is not contained in the measurements used to estimate the SCM. Monzingo and Miller show that when the signal is included, the number of snapshots required to achieve the ensemble performance is a function of the signal-to-noise ratio (SNR) [3].

For large arrays or fast-changing environments, it is difficult to obtain the required number of snapshots because the data are not stationary over long enough time intervals. These cases require beamformers that achieve faster convergence by reducing the adaptive degrees of freedom. One class of adaptive methods relies on an eigendecomposition of the SCM. In his comprehensive reference on array processing, Van Trees indicates that there are two main types of eigenvector beamforming algorithms [4, pp. 556–576]. The first type, which Van Trees calls the "eigenspace beamformer," projects the data into a subspace formed from the eigenvectors associated with the largest eigenvalues, e.g., see [5]–[7]. The second type of algorithm is dominant mode rejection (DMR) [8], which is the focus of this paper. Instead of projecting into a reduced-rank subspace, DMR uses the eigendecomposition to define a subspace containing the dominant interferers that it wants to reject, thereby allowing it to detect low-power signals. The DMR weight vector has the same form as the MVDR weight vector, but the DMR ABF replaces the SCM with a structured estimate constructed from the eigendecomposition of the SCM.

While a number of papers explore how to make DMR robust to mismatch [9]–[13] and investigate its performance using experimental data [14], few consider the snapshot performance of the algorithm. There are no analytical expressions (similar to those in [2] and [3]) that predict the number of snapshots DMR requires to achieve a specific level of performance. Two papers, authored by Messerschmidt and Gramann [15] and Redheendran and Gramann [16], investigate DMR performance using

Manuscript received August 02, 2012; revised January 14, 2013; accepted March 01, 2013. Date of publication May 14, 2013; date of current version April 10, 2014. This work was supported by the U.S. Office of Naval Research under Code 321 US through awards N00014-09-1-0114, N00014-12-1-0048, N00014-09-1-167, and N00014-12-1-0047.

Associate Editor: D. A. Abraham.

K. E. Wage is with the Department of Electrical and Computer Engineering, George Mason University, Fairfax, VA 22030 USA (e-mail: k.e.wage@ieee.org).

J. R. Buck is with the Department of Electrical and Computer Engineering, University of Massachusetts Dartmouth, North Dartmouth, MA 02747 USA (e-mail: johnbuck@ieee.org).

Color versions of one or more of the figures in this paper are available online at http://ieeexplore.ieee.org.

Digital Object Identifier 10.1109/JOE.2013.2251538

deep- and shallow-water sonar data sets. The experimental analysis of beam noise in these papers supports the claim that the DMR ABF requires fewer snapshots than the MVDR ABF to achieve the same performance, but these papers do not extend the empirical results to predict the relationship between snapshots and performance for an arbitrary array. Van Trees discusses how the output SINR of the DMR ABF varies with snapshots for a specific example using a ten-sensor array, but he does not derive analytic expressions for SINR, nor does he draw general conclusions about algorithm performance [4, pp. 845–850].

While no analysis comparable to that of Reed *et al.* [2] exists for the DMR ABF, Chang and Yeh [6] and Feldman and Griffiths [7] analyze the snapshot performance of eigenspace beamformers. Eigenspace ABFs require the desired signal to be loud enough that it is included in the reduced-rank subspace used for the projection, whereas the DMR ABF depends on the desired signal being quiet enough that it is not included in its dominant interferer subspace. The difference in assumptions leads to a fundamental performance difference between DMR and other eigenspace methods, particularly when the subspace must be estimated from the SCM. See Van Trees [4, pp. 845–850] for examples illustrating why the results for eigenspace beamformers are not directly applicable to DMR.

The goal of this paper is to investigate the snapshot performance of the DMR ABF. The analysis focuses on the fundamental case of a single interferer in white noise. While the single-interferer assumption is unrealistic in practice, a thorough understanding of this simplified case provides valuable insights and is a necessary first step in the analysis of more complex scenarios. Theoretical calculations for the ensemble DMR ABF reveal the relationships among notch depth, white noise gain, and SINR. The centerpiece of the paper is a detailed empirical study of the single-interferer case. This study quantifies how DMR performance varies with the number of snapshots used to estimate the SCM. It also demonstrates that the sample eigenvectors have a greater effect on performance than the sample eigenvalues.

An important aspect of the simulation study is that it includes scenarios with fewer snapshots than sensors. A significant limitation of previous work on eigenspace ABFs is the assumption that the number of snapshots exceeds the number of sensors. The theoretical predictions derived by Chang and Yeh [6] and Feldman and Griffiths [7] rely on asymptotic calculations where the number of snapshots approaches infinity while the array size remains fixed. This type of asymptotic analysis is not relevant for large arrays, which almost always operate with fewer snapshots than sensors. Fortunately, new mathematical results in the area of random matrix theory (RMT) offer the opportunity to analyze the snapshot-deficient cases that are of practical interest. RMT characterizes the statistical behavior of the eigenvalues and eigenvectors of large random matrices [17]. In contrast to the previous asymptotic approach, RMT allows both the number of sensors and snapshots to grow to infinity, while holding their ratio fixed. Since the RMT results converge relatively quickly with respect to the number of sensors, it is possible to use the theory to analyze arrays of moderate size. This paper interprets the snapshot behavior of the DMR ABF using the recent results of Paul [18], Nadler [19], Johnstone and Lu [20], and Benaych-Georges and Nadakuditi [21] on the eigenvalues and eigenvectors of the *spiked covariance model*. This model is identical to the structured SCM assumed in DMR processing, i.e., the data consist of several dominant interferers plus spatially white noise.

The paper is organized as follows. Section II gives an overview of the beamforming problem, reviews standard metrics used to assess beamformer performance, and presents the DMR beamformer. Section III derives the notch depth, white noise gain, and SINR for the ensemble DMR ABF. Section IV presents the simulation study of DMR performance as a function of the number of snapshots used to estimate the SCM. Using the same large set of simulations, Section V examines the relative influence of the sample eigenvalues and eigenvectors on DMR notch depth. Section VI interprets the empirical results using insights drawn from RMT. Section VII relates the conclusions drawn from the DMR study to results for other ABFs. Section VIII summarizes the paper and briefly discusses topics for future work.

II. Background

Abraham and Owsley introduced the DMR ABF in 1990 [8]. As noted in the introduction, other authors derived variations of the DMR beamformer to address problems such as mismatch, e.g., the work of Cox *et al.* [9], [10]. The following section briefly reviews essential background on the beamforming problem and discusses several important performance metrics. Section II-B defines the version of the DMR beamformer used throughout this paper.

This paper uses the following notational conventions. Bold lowercase letters denote vectors, and bold uppercase vectors denote matrices. Nonbold letters are scalars. Greek letters represent ensemble quantities, and roman letters represent estimated quantities, e.g., $\mathbf{\Sigma}$ is the ECM and $\mathbf{S}$ is the SCM. Superscript H denotes the Hermitian transpose.

A. Planewave Beamforming and Performance Metrics

This section provides a brief overview of narrowband planewave beamforming. For a thorough treatment of the subject, see the textbook by Van Trees [4]. The notation introduced below is consistent with [4].

Planewave beamforming assumes that the data measured by an array consist of one or more planewave signals plus noise. For a narrowband beamformer, the signal received by an array can be written as a column vector

$$\mathbf{p} = \sum_{i=1}^{D} b_i \mathbf{v}_i + \mathbf{n} \tag{1}$$

where D is the number of planewave signals, b_i is the amplitude of the ith signal, $\mathbf{v}_i$ is the planewave replica vector for the ith signal, and $\mathbf{n}$ is a vector of complex noise samples. For an N-sensor linear array oriented along the z-axis, the replica for the ith signal is a complex exponential vector

$$\mathbf{v}_i = \mathbf{v}(\theta_i) = \begin{bmatrix} e^{j\frac{2\pi}{\lambda}\cos(\theta_i)z_1} \\ \vdots \\ e^{j\frac{2\pi}{\lambda}\cos(\theta_i)z_N} \end{bmatrix} \tag{2}$$

where λ is the wavelength, θ_i is the planewave angle measured from the positive z-axis, and z_n is the location of the nth sensor. Note that the replica is normalized such that $\mathbf{v}_i^{\mathrm{H}}\mathbf{v}_i = N$. This paper assumes that the signal amplitude b_i is a zero-mean complex circular random variable and that the complex circular random noise is zero mean and spatially white. Assuming that the planewave signals are independent, the ECM for the received signal is

$$\mathbf{\Sigma} = \mathcal{E}\{\mathbf{p}\mathbf{p}^{\mathrm{H}}\} = \sum_{i=1}^{D} \sigma_i^2 \mathbf{v}_i \mathbf{v}_i^{\mathrm{H}} + \sigma_w^2 \mathbf{I}. \tag{3}$$

The power in the ith source is σ_i^2, and the white noise power is σ_w^2.

The goal of beamforming is to process the received vector $\mathbf{p}$ such that a planewave signal from a desired direction θ_m passes through undistorted while signals from other angles are attenuated. The output of a linear beamformer is $\mathbf{w}^{\mathrm{H}}\mathbf{p}$, where $\mathbf{w}$ is the weight vector associated with the steering angle θ_m. The conventional beamformer is the spatial matched filter for the replica vector associated with the steering direction, i.e., the CBF weight vector is

$$\mathbf{w}_{\mathrm{CBF}} = \frac{1}{N}\mathbf{v}_m = \frac{1}{N}\mathbf{v}(\theta_m). \tag{4}$$

The $1/N$ normalization guarantees that the CBF has unity gain in the look direction.

The remainder of this section reviews standard metrics of beamformer performance. Each of the metrics defined below depends on the weight vector $\mathbf{w}$, which depends on the steering angle θ_m. To keep the notation simple, the dependence on θ_m is not explicitly included in the definitions. Note that for data-dependent (adaptive) weight vectors, the following metrics are also data dependent, thus they can be modeled as random variables and quantified by their statistics (mean, variance, etc.).

The first metric of interest is the beampattern, which is defined in terms of the angle θ or, equivalently, in terms of its cosine $u = \cos(\theta)$

$$B(\theta) \triangleq \mathbf{w}^{\mathbf{H}}\mathbf{v}(\theta) = \mathbf{w}^{\mathrm{H}}\mathbf{v}(u). \tag{5}$$

The beampattern is analogous to the frequency response of a filter. It quantifies the beamformer's response to a unity amplitude planewave from angle θ. Note that the weight vector $\mathbf{w}$ depends on the steering angle θ_m, but this dependence is suppressed in (5) and all subsequent equations to simplify the notation.

Since one purpose of a beamformer is to eliminate loud signals coming from angles other than the steering direction, it is important to quantify how much the beamformer attenuates these interferers. The notch depth (ND) is defined as the absolute value squared of the beampattern in the direction of an interfering signal, e.g., for the ith interferer

$$\mathrm{ND} \triangleq |B(\theta_i)|^2 = |\mathbf{w}^{\mathrm{H}}\mathbf{v}_i|^2. \tag{6}$$

ND is associated with a particular interference direction θ_i; it is not necessarily associated with a minimum in the beampattern.

White noise gain (WNG) is a standard metric that quantifies the improvement in the SNR provided by a beamformer when the noise is spatially white. It is defined as

$$\mathrm{WNG} \triangleq \frac{1}{\mathbf{w}^{\mathrm{H}}\mathbf{w}}. \tag{7}$$

WNG is a useful indicator of how robust a beamformer is to array perturbations or mismatch. The CBF has the optimal WNG, which is equal to the number of sensors (N).

The final two metrics of interest are SINR and SINR loss. The SINR of a beamformer is defined as

$$\mathrm{SINR} \triangleq \frac{\sigma_s^2 |\mathbf{w}^{\mathrm{H}}\mathbf{v}_s|^2}{\mathbf{w}^{\mathrm{H}}\mathbf{\Sigma}_{\mathrm{I+N}}\mathbf{w}} \tag{8}$$

where σ_s^2 is the desired signal power, $\mathbf{v}_s$ is the replica associated with the desired signal, and $\mathbf{\Sigma}_{\mathrm{I+N}}$ is the ensemble interference-plus-noise covariance matrix. This definition uses the ensemble $\mathbf{\Sigma}_{\mathrm{I+N}}$ rather than the sample covariance because it produces a smoother result when the SINR must be estimated from sample realizations of the weight vector [4, p. 732]. SINR loss is defined as the ratio of the SINR for an ABF designed using L snapshots to the SINR obtained for a beamformer designed using ensemble statistics

$$\rho \triangleq \frac{\mathrm{SINR}}{\mathrm{SINR}_{\mathrm{ens}}}. \tag{9}$$

Note that $0 \leq \rho \leq 1$.

B. DMR Beamformer

To derive the DMR ABF, Abraham and Owsley start with a general model for $\mathbf{p}$ that includes discrete planewave signals, colored noise, and spatially white noise with power σ_w^2 [8]. They assume that there are D strong planewave signals (interferers) that need to be attenuated to facilitate detection of a weaker desired planewave signal. With this assumption, they can partition the covariance matrix into a dominant interferer subpace and a noise subspace; the latter includes the weaker signals and the noise. DMR assumes that the large eigenvalues of $\mathbf{\Sigma}$ are all associated with interferers to be rejected and that the small eigenvalues are due to weak signals and noise. Sorting the eigenvalues in descending order leads to the following expression for the eigendecomposition of the ECM:

$$\mathbf{\Sigma} = \mathbf{\Xi}\mathbf{\Gamma}\mathbf{\Xi}^{\mathrm{H}} = \underbrace{\sum_{n=1}^{D} \gamma_n \boldsymbol{\xi}_n \boldsymbol{\xi}_n^{\mathrm{H}}}_{\text{large eigenvalues}} + \underbrace{\sum_{n=D+1}^{N} \gamma_n \boldsymbol{\xi}_n \boldsymbol{\xi}_n^{\mathrm{H}}}_{\text{eigenvalues}} \tag{10}$$

where γ_n is the nth eigenvalue and $\boldsymbol{\xi}_n$ is the corresponding eigenvector. The eigenvectors corresponding to the D largest eigenvalues define the dominant subspace. The DMR ABF forms a structured approximation to $\mathbf{\Sigma}$ using the dominant subspace plus an orthogonal noise subspace with equal power (σ_w^2) in each noise direction, i.e.,

$$\mathbf{\Sigma}_{\mathrm{DMR}} = \sum_{n=1}^{D} \gamma_n \boldsymbol{\xi}_n \boldsymbol{\xi}_n^{\mathrm{H}} + \sum_{n=D+1}^{N} \sigma_w^2 \boldsymbol{\xi}_n \boldsymbol{\xi}_n^{\mathrm{H}}. \tag{11}$$

The DMR weight vector is the MVDR weight vector [1], with the ECM replaced by $\mathbf{\Sigma}_{\mathrm{DMR}}$

$$\mathbf{w}_{\mathrm{DMR}} = \left(\mathbf{v}_m^{\mathrm{H}}\mathbf{\Sigma}_{\mathrm{DMR}}^{-1}\mathbf{v}_m\right)^{-1}\mathbf{\Sigma}_{\mathrm{DMR}}^{-1}\mathbf{v}_m \tag{12}$$

where $\mathbf{v}_m$ is the replica associated with the steering angle θ_m.

In practice, the ECM is not available, so $\mathbf{\Sigma}_{\mathrm{DMR}}$ cannot be constructed. Instead, the structured covariance matrix required for DMR is computed using the SCM based on L snapshots. The SCM and its eigendecomposition are defined as

$$\mathbf{S} = \frac{1}{L}\sum_{l=1}^{L}\mathbf{p}_l\mathbf{p}_l^{\mathrm{H}} = \sum_{n=1}^{N} g_n\mathbf{e}_n\mathbf{e}_n^{\mathrm{H}} = \mathbf{E}\mathbf{G}\mathbf{E}^{\mathrm{H}} \tag{13}$$

where $\mathbf{p}_l$ is the lth data snapshot, and $\mathbf{e}_n$ and g_n are the sample eigenvectors and eigenvalues, respectively. Using the SCM, the sample DMR covariance matrix is

$$\mathbf{S}_{\mathrm{DMR}} = \sum_{n=1}^{D} g_n\mathbf{e}_n\mathbf{e}_n^{\mathrm{H}} + \sum_{n=D+1}^{N} s_w^2\mathbf{e}_n\mathbf{e}_n^{\mathrm{H}} \tag{14}$$

where s_w^2 is the estimated noise power

$$s_w^2 = \left(\frac{L}{L-1}\right)\left(\frac{1}{N-D}\right)\sum_{n=D+1}^{N} g_n. \tag{15}$$

The $L/(L-1)$ factor in (15) compensates for the inherent bias in sample variance calculations. This factor is negligible when L is large, but must be included to obtain unbiased results for snapshot-deficient cases. The advantage of using the estimated noise power when computing $\mathbf{S}_{\mathrm{DMR}}$ is that it eliminates the small eigenvalues, which cause problems with inverting the SCM to compute the MVDR weight vector.

Substituting $\mathbf{S}_{\mathrm{DMR}}$ for $\mathbf{\Sigma}_{\mathrm{DMR}}$ in (12) and using the matrix inversion lemma, the DMR weight vector can be written

$$\mathbf{w}_{\mathrm{DMR}} = \frac{\mathbf{v}_m - \sum_{i=1}^{D}\left(\frac{g_i - s_w^2}{g_i}\right)\mathbf{e}_i\mathbf{e}_i^{\mathrm{H}}\mathbf{v}_m}{\mathbf{v}_m^{\mathrm{H}}\mathbf{v}_m\left(1 - \sum_{i=1}^{D}\left(\frac{g_i - s_w^2}{g_i}\right)\cos^2(\mathbf{e}_i, \mathbf{v}_m)\right)}. \tag{16}$$

$\cos^2(\mathbf{e}_i, \mathbf{v}_m)$ is the generalized cosine between vectors $\mathbf{e}_i$ and $\mathbf{v}_m$, as defined in [22].

As discussed in Section I, several authors consider modifications of the basic DMR ABF to address issues of robustness [9]–[13]. While a thorough discussion of robust DMR is beyond the scope of this paper, it is important to note that all the modified DMR algorithms exclude an eigenvector from the dominant subspace when its associated interferer moves too close to the desired look direction. Attenuating a loud signal that is inside the mainlobe (ML) of the beamformer while maintaining the unity gain constraint is quite difficult. This problem is not unique to DMR; the performance of most ABFs degrades substantially in the presence of ML interference if the proper adjustments are not made [4, pp. 471–472].

TABLE I
PARAMETERS OF CANONICAL SINGLE-INTERFERER EXAMPLE

Number of sensors	$N = 50$
Sensor spacing	half-wavelength
Steering direction	broadside, $u_m = \cos(\theta_m) = 0$
Interferer location	$u_1 = \cos(\theta_1) = 3/N = 0.06$
DMR subspace dimension	$D = 1$

III. Ensemble Performance for the Single-Interferer Example

The remainder of the paper focuses on an illustrative example of a single planewave interferer in spatially white noise. For simplicity, the example also assumes that the measured data do not contain a desired signal arriving from the steering direction. Although these assumptions are unrealistic in practice, this example facilitates a fundamental analysis of the DMR ABF's ability to remove interference. A thorough understanding of this single-interferer example is required before considering more realistic multiple-interferer scenarios. This section derives the ensemble performance of the DMR ABF for the single-interferer example. The ensemble results provide a baseline for comparison in the later sections that consider the snapshot performance of the DMR ABF.

For a single interferer, the expression for the ECM in (3) simplifies to

$$\mathbf{\Sigma} = \sigma_1^2\mathbf{v}_1\mathbf{v}_1^{\mathrm{H}} + \sigma_w^2\mathbf{I}. \tag{17}$$

In this case, it is easy to show (cf. [23, pp. 617–618]) that the maximum eigenvalue of the covariance matrix is $\gamma_1 = N\sigma_1^2 + \sigma_w^2$ and the rest of the eigenvalues are $\gamma_{n\neq 1} = \sigma_w^2$. The eigenvector associated with the maximum eigenvalue is $\boldsymbol{\xi}_1 = \mathbf{v}_1/\sqrt{N}$. The interference-to-noise ratio (INR) is defined as σ_1^2/σ_w^2.

Table I summarizes the parameters of the canonical single-interferer example used throughout the paper. The example uses a 50-sensor equispaced linear array with half-wavelength spacing. The array is steered to broadside, and the interferer is located near the peak sidelobe of the CBF. The directional cosine associated with the interferer is $u_1 = \cos(\theta_1) = 3/N = 0.06$. For all results described below, the DMR subspace dimension D is set to one. INR is a simulation variable.

A. Ensemble Beampattern

Substituting the ensemble statistics into (16) and rearranging, the DMR weight vector for the single-interferer case is

$$\mathbf{w}_{\mathrm{DMR}} = \frac{\left(\mathbf{I} - \boldsymbol{\xi}_1\boldsymbol{\xi}_1^{\mathrm{H}}\right)\mathbf{v}_m + \left(\frac{\sigma_w^2}{\gamma_1}\boldsymbol{\xi}_1\boldsymbol{\xi}_1^{\mathrm{H}}\right)\mathbf{v}_m}{N\left(1 - \left(\frac{\gamma_1 - \sigma_w^2}{\gamma_1}\right)\cos^2(\boldsymbol{\xi}_1, \mathbf{v}_m)\right)}. \tag{18}$$

The above expression relies on the normalization of the replica vectors ($\|\mathbf{v}\|^2 = N$) defined in Section II-B. Fig. 1 shows the ensemble DMR beampattern for the canonical single-interferer example when the INR is 40 dB. The beampattern is plotted

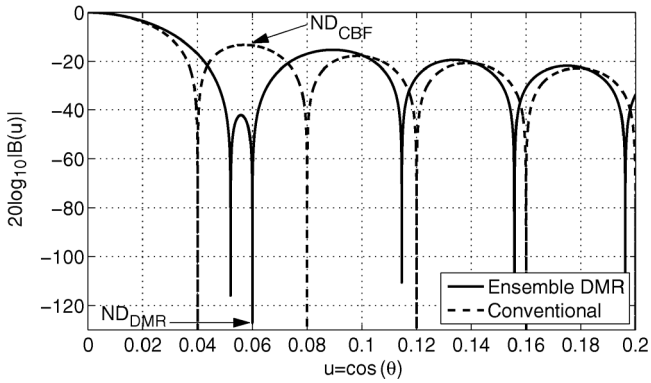

Fig. 1. Ensemble DMR beampattern for the canonical single-interferer example. The interferer location is $u_1 = 0.06$ (see Table I), and the INR is 40 dB. The CBF beampattern is shown for comparison. Arrows indicate the ND for both beamformers.

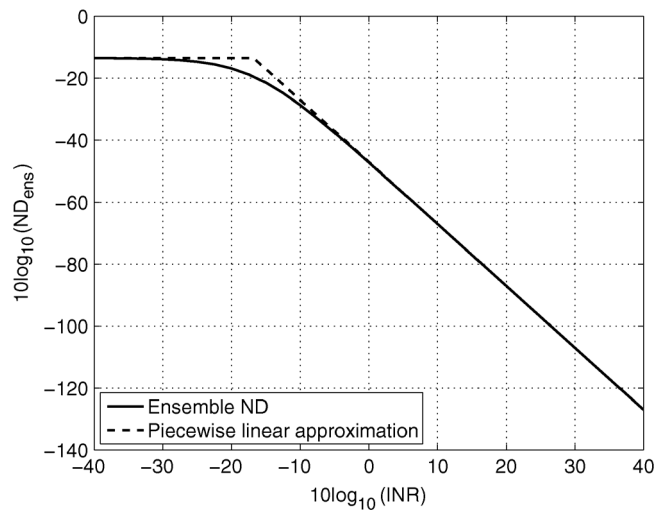

Fig. 2. Ensemble DMR ND (solid line) as a function of INR for the canonical single-interferer example. The dashed line shows the piecewise linear approximation to the ensemble ND.

as a function of the directional cosine $u = \cos(\theta)$. Compared to the beampattern of a uniformly weighted CBF (dashed line), the ensemble DMR beampattern (solid line) has a deep notch at the location of the interferer $(u_1 = 0.06)$, when the array is steered to broadside. Note that this paper distinguishes between a notch and a null. According to Van Trees [4, p. 471], a null is a point where the beampattern is exactly equal to zero, whereas a notch is a "partial null," which is not a zero crossing of the beampattern. As defined in Section II-A, ND is the absolute value squared of the beampattern at the interference direction (u_1 in this case). It quantifies how much the interference will be attenuated compared to the desired signal that passes with unity gain. The ND of the ensemble DMR ABF is -127.0 dB for this example. The CBF beampattern does not have a drop near u_1 because the example was designed to locate the interferer near the peak sidelobe of the conventional beamformer. While there is no real notch in the CBF, $\mathrm{ND_{CBF}}$ is still defined as $|B_{\mathrm{CBF}}(u_1)|^2$. The ND of the CBF for this example is -13.5 dB.

B. Ensemble Notch Depth

A general formula for the ensemble DMR ND in the single-interferer case is derived by evaluating (6) using the weight vector in (18)

$$\mathrm{ND_{ens}} = \left|\mathbf{w}_{\mathrm{DMR}}^{\mathrm{H}}\mathbf{v}_1\right|^2 = \frac{\cos^2(\boldsymbol{\xi}_1, \mathbf{v}_m)}{\left(1 + N\dfrac{\sigma_1^2}{\sigma_w^2}\sin^2(\boldsymbol{\xi}_1, \mathbf{v}_m)\right)^2} \quad (19)$$

where $\sin^2(\boldsymbol{\xi}_1, \mathbf{v}_m) = 1 - \cos^2(\boldsymbol{\xi}_1, \mathbf{v}_m)$ is the generalized sine squared [22]. When the INR is small, (19) shows that ND is equal to $\cos^2(\boldsymbol{\xi}_1, \mathbf{v}_m)$, which is the ND provided by the uniformly weighted CBF. As INR increases, ND starts to roll off. At high INRs, $\mathrm{ND_{ens}}$ decreases by 20 dB for every 10-dB increase in INR. Fig. 2 illustrates this behavior using the canonical single-interferer example. The solid line shows how $\mathrm{ND_{ens}}$ varies with INR on a log–log plot. A piecewise linear approximation of $\mathrm{ND_{ens}}$ can be constructed using an approach similar to that used to create Bode plots of the magnitude response of linear time-invariant systems. The numerator of (19) is the CBF ND, which corresponds to a constant offset. The denominator contributes 0 dB up until the breakpoint defined by INR $= 1/(N\sin^2(\boldsymbol{\xi}_1, \mathbf{v}_m))$. For INRs higher than the breakpoint, the denominator corresponds to a 20-dB/decade decrease in ND. The dashed line in Fig. 2 shows the straight-line approximation to $\mathrm{ND_{ens}}$. The maximum error between the approximation and the true curve occurs at the breakpoint and is approximately equal to 6 dB.

C. Ensemble White Noise Gain

Using (18) in (7), the ensemble DMR WNG for the single-interferer example is

$$\mathrm{WNG_{ens}} = \frac{N\left(1 + N\dfrac{\sigma_1^2}{\sigma_w^2}\sin^2(\boldsymbol{\xi}_1, \mathbf{v}_m)\right)^2}{1 + 2N\dfrac{\sigma_1^2}{\sigma_w^2}\sin^2(\boldsymbol{\xi}_1, \mathbf{v}_m) + \left(N\dfrac{\sigma_1^2}{\sigma_w^2}\right)^2\sin^2(\boldsymbol{\xi}_1, \mathbf{v}_m)}. \quad (20)$$

Dividing the numerator and the denominator of (20) by the numerator and rearranging yields

$$\mathrm{WNG_{ens}} = \frac{N}{1 + \dfrac{\left(N\dfrac{\sigma_1^2}{\sigma_w^2}\right)^2\sin^2(\boldsymbol{\xi}_1, \mathbf{v}_m)\cos^2(\boldsymbol{\xi}_1, \mathbf{v}_m)}{\left(N\dfrac{\sigma_1^2}{\sigma_w^2}\right)^2\sin^4(\boldsymbol{\xi}_1, \mathbf{v}_m) + 2N\dfrac{\sigma_1^2}{\sigma_w^2}\sin^2(\boldsymbol{\xi}_1, \mathbf{v}_m) + 1}}. \quad (21)$$

When the INR is large, only the leading order terms in the denominator fraction matter. In this case, the expression reduces to

$$\mathrm{WNG_{asympt}} = \frac{N}{1 + \cot^2(\boldsymbol{\xi}_1, \mathbf{v}_m)} \quad (22)$$

where $\cot^2$ is defined as the square of the ratio of the generalized cosine and sine. The factor of $1/(1 + \cot^2)$ predicts the loss in WNG of the ensemble DMR ABF as compared to the optimal WNG of N. This loss can be interpreted as the cost of placing a notch in the beampattern in the direction of the interferer. The loss factor is only a function of the interferer location relative to

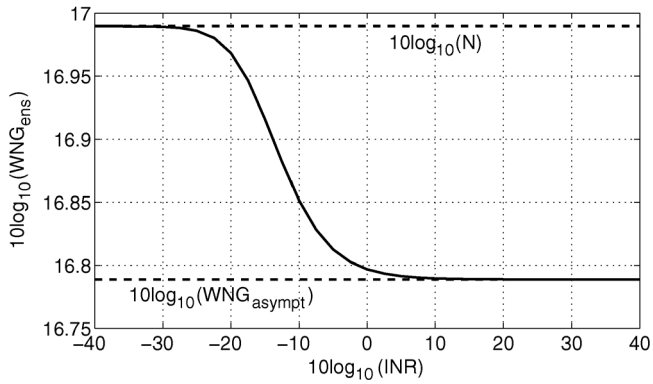

Fig. 3. Ensemble DMR WNG as a function of INR for the canonical single-interferer example. The solid line shows the results for the single interferer located near the peak sidelobe of the CBF. The dashed lines show the optimal WNG (N) and the large INR approximation derived in (22).

the look direction and not a function of the INR. For interferers outside the ML, $\cot^2$ is small and the loss in WNG is minimal. Fig. 3 shows the ensemble WNG as a function of INR for the canonical single-interferer example. The plot illustrates how the WNG smoothly transitions between the optimal value of N for low INR and the $\text{WNG}_{\text{asympt}}$ value for high INR. Since the interferer is outside the ML, the maximum loss in WNG is small (on the order of 0.2 dB).

D. Ensemble SINR

For the single-interferer example, the ensemble SINR can be written as a function of ND and WNG. Substituting the ECM defined in (17) into (8) yields

$$\text{SINR}_{\text{ens}} = \frac{\frac{\sigma_s^2}{\sigma_w^2}|\mathbf{w}^{\text{H}}\mathbf{v}_s|^2}{\frac{\sigma_1^2}{\sigma_w^2}|\mathbf{w}^{\text{H}}\mathbf{v}_1|^2 + \mathbf{w}^{\text{H}}\mathbf{w}}. \tag{23}$$

Assuming that the ABF is steered toward the true source direction, $|\mathbf{w}^{\text{H}}\mathbf{v}_s|^2$ equals 1. In this case, the SINR is

$$\text{SINR}_{\text{ens}} = \frac{\text{SNR}}{\text{INR}\cdot\text{ND}_{\text{ens}} + 1/\text{WNG}_{\text{ens}}} \tag{24}$$

where $\text{SNR} = \sigma_s^2/\sigma_w^2$. The two terms in the denominator represent the power of the interferer and the power of the white noise at the output of the ABF. Fig. 4 plots these terms as a function of INR for the canonical single-interferer example. It is easy to bound the output interferer power using piecewise linear approximations for INR and ND. In Fig. 4, the solid line is INR · ND and the dash–dot line is the straight-line approximation to this term. At its worst, the approximation is 6 dB larger than the true value (due to the error in the ND approximation); the maximum deviation occurs at the breakpoint. The peak value of INR · ND over all INR occurs at the breakpoint and is equal to

$$\max_{\text{INR}}\{\text{INR}\cdot\text{ND}\} = \frac{\cos^2(\boldsymbol{\xi}_1, \mathbf{v}_m)}{4N\sin^2(\boldsymbol{\xi}_1, \mathbf{v}_m)} = \frac{\cot^2(\boldsymbol{\xi}_1, \mathbf{v}_m)}{4N}. \tag{25}$$

For the case presented in Fig. 4, the interferer power at the output of the ensemble DMR ABF (solid line) is always less

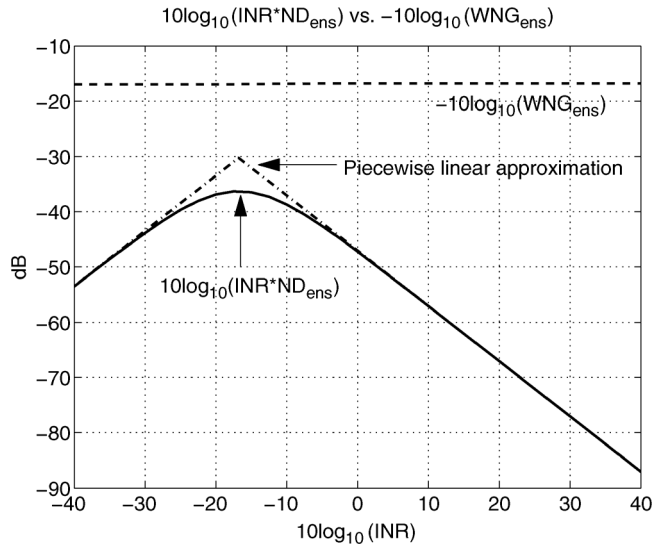

Fig. 4. Comparison of the interferer and white noise terms in the denominator of the SINR equation for the ensemble DMR ABF. Results are shown for the canonical single-interferer example.

than the white noise power (dashed line). When this is true, the SINR is primarily controlled by the white noise term rather than the interferer. It is useful to derive the condition that guarantees $\text{INR}\cdot\text{ND}_{\text{ens}} < 1/\text{WNG}_{\text{ens}}$. Based on the discussion in Section III-C, the largest that WNG_{ens} can be is N, thus the smallest that $1/\text{WNG}_{\text{ens}}$ can be is $1/N$. Comparing the maximum value for $\text{INR}\cdot\text{ND}_{\text{ens}}$ from (25) and the minimum value for $1/\text{WNG}_{\text{ens}}$ yields

$$\frac{\cot^2(\boldsymbol{\xi}_1, \mathbf{v}_m)}{4N} < \frac{1}{N} \tag{26}$$

which reduces to

$$\cot^2(\boldsymbol{\xi}_1, \mathbf{v}_m) < 4. \tag{27}$$

Since $\cot^2(\boldsymbol{\xi}_1, \mathbf{v}_m) < 1$ for values outside the 3-dB point of the ML, the white noise term is guaranteed to be at least 6 dB larger than the interferer term for interferers located outside the ML of the CBF. Thus, as long as the interferer is not too close to the look direction, the ensemble DMR ABF is guaranteed to have a notch deep enough to make the interferer irrelevant. In this case, the ensemble SINR is approximately

$$\text{SINR}_{\text{ens}} \approx \text{SNR}\cdot\text{WNG}_{\text{ens}} \quad \text{(interferer outside ML)}. \tag{28}$$

IV. Snapshot Performance for the Single-Interferer Example

This section investigates the performance of the DMR ABF as a function of the number of snapshots available to estimate the SCM and its corresponding eigendecomposition. Specifically, it presents the results of an empirical study characterizing ND, WNG, and SINR for a single interferer in spatially white noise. The simulations use the canonical example introduced in Section III (see Table I). Both the interferer and the noise are modeled as complex circular Gaussian random variables. Histograms and other estimated statistics are based on 3000 Monte Carlo trials.

The study considers cases ranging from $L = 2$ to 50 000 snapshots. DMR requires at least two snapshots for the single-interferer example since it needs an estimate of the dominant subspace and an estimate of the power in the noise subspace. The dominant subspace is defined by the eigenvector associated with the maximum eigenvalue. With two snapshots, the noise power is simply a scaled version of the only other nonzero eigenvalue [see (15)]. Although obtaining 50 000 snapshots is unrealistic in practice, this case is included to illustrate performance as L gets large. In some plots, the performance for $L = 100 = 2N$ snapshots is also highlighted since $2N$ snapshots is the "rule of thumb" for acceptable performance [4, p. 733]. The rule is based on the analysis of the MVDR ABF by Reed *et al.* [2].

A. Sample Beampatterns

Fig. 5 shows sample DMR beampatterns for the case of a strong interferer; the INR is 40 dB. Fig. 5(a) compares the DMR beampatterns generated using ensemble and sample statistics with the beampattern of a uniformly weighted CBF. All the DMR beampatterns have a notch near the interferer location u_1. Fig. 5(b) zooms in around the interferer to show the depth of the DMR notches. The DMR ABFs designed using 2 and 100 snapshots have notches of -59.1 and -76.2 dB, respectively. The ensemble DMR ABF, generated using the ECM, has a substantially lower notch of -127.0 dB. Note that while the ensemble beampattern has a minimum at the interferer angle, the sample beampatterns have minima at slightly different angles due to the mismatch in the sample statistics. These sample minima are not as small as the ensemble minimum.

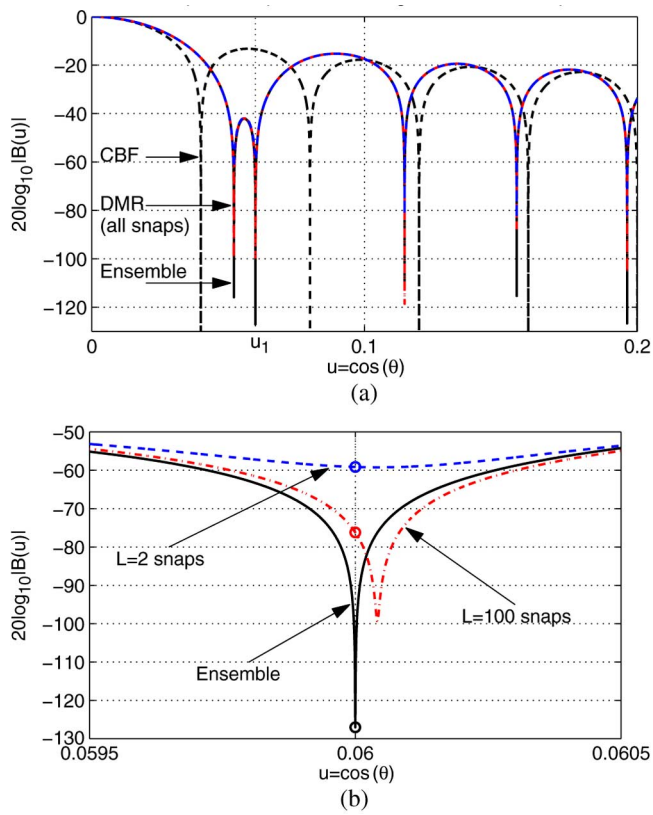

Fig. 5. Comparison of beampatterns for the conventional and DMR beamformers for the canonical example when the INR is 40 dB. The plots show results for the DMR beamformers generated with the ensemble covariance, as well as for the sample covariances estimated with 2 and 100 snapshots. (a) Conventional and DMR beampatterns for single-interferer example. (b) Closeup of DMR beampatterns around interferer location. Circles highlight the NDs at the angle of the interferer.

B. Notch Depth Statistics

This section characterizes the variability of the DMR ND for the single-interferer example using a large set of Monte Carlo trials. Fig. 6 shows histograms of ND for an interferer with 40-dB INR. The figure compares the NDs for the DMR ABFs generated with 2 and 500 snapshots. Fig. 6 highlights several important points about DMR ND. First, the ND distributions are unimodal and slightly asymmetric. The tail on the left (lower notch values) is longer than the tail on the right (higher notch values). Second, DMR ND improves with a larger number of snapshots, as expected. The mean ND for the $L = 500$ case is 26.8 dB lower than the mean for the $L = 2$ case. While performance improves with snapshots, it is important to note that the mean ND with 500 (10 N) snapshots is still 43.3 dB away from the ensemble result. The ensemble prediction is overly optimistic and unlikely to be achievable in practice.

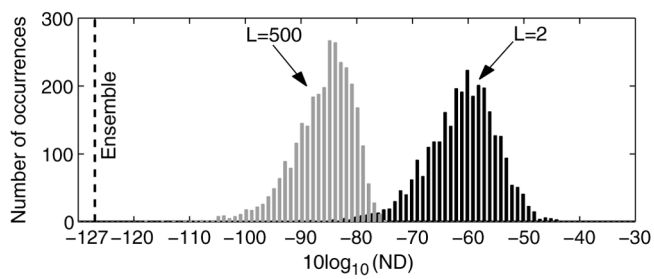

Fig. 6. Histograms of DMR ND for the canonical example when the INR is 40 dB. Results are shown for DMR ABFs generated using 2 and 500 snapshots. The dashed line indicates the ND achievable with ensemble statistics.

Fig. 7 shows how ND varies with INR for the cases of 2, 100, and 50 000 snapshots. The CBF and ensemble DMR results are included for reference. Each curve represents a different number of snapshots. The symbols denote the mean ND and the error bars indicate the spread of the distribution between the 10th and 90th percentiles. The error bars are asymmetric around the mean, as expected from the histograms in Fig. 6. Fig. 7 illustrates several important points. First, at very low INR, the ND for all the snapshot cases converges to the uniformly weighted CBF result. This agrees with the ensemble prediction. Second, while all the curves show a rolloff of ND with increasing INR, the slope of the curves does not always agree with the slope of the ensemble prediction. For low numbers of snapshots ($L = 2$, 100), the slope is equal to -1, i.e., 10-dB decrease for every 10 dB of INR. This does not agree with the ensemble slope of -2. For higher numbers of snapshots (such as the $L = 50\,000$ case shown), the slope is equal to -2 for low INRs and switches to -1 for higher INRs. The threshold at which the slope change occurs depends on the number of snapshots.

When implementing the DMR ABF, it is useful to know the number of snapshots required to achieve a specific level of performance. Based on the same set of Monte Carlo trials as Fig. 7, Fig. 8 displays ND as a function of snapshots for five different INRs. Similar to Fig. 7, the symbols denote the mean ND and the error bars indicate the spread of the distribution between the 10th and 90th percentiles. The solid symbols on the right-hand

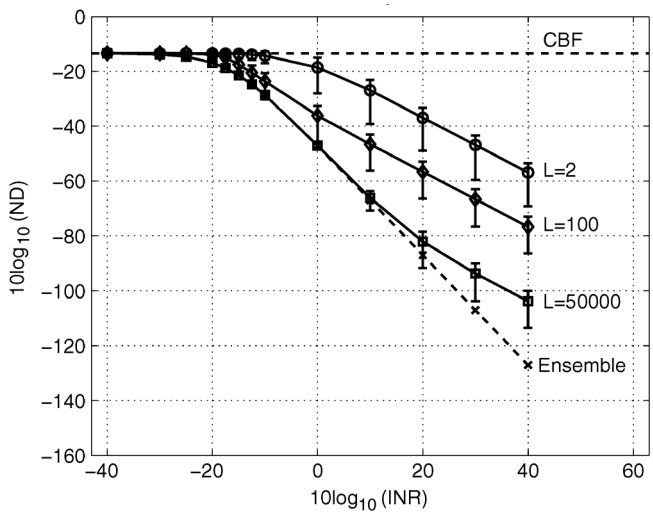

Fig. 7. DMR ND as a function of INR for the canonical example. Results are shown for DMR ABFs generated using three different numbers of snapshots and for the ensemble DMR ABF. The symbols denote the mean ND and the error bars mark the span between the 10th and 90th percentiles of the data. The CBF ND is included for reference.

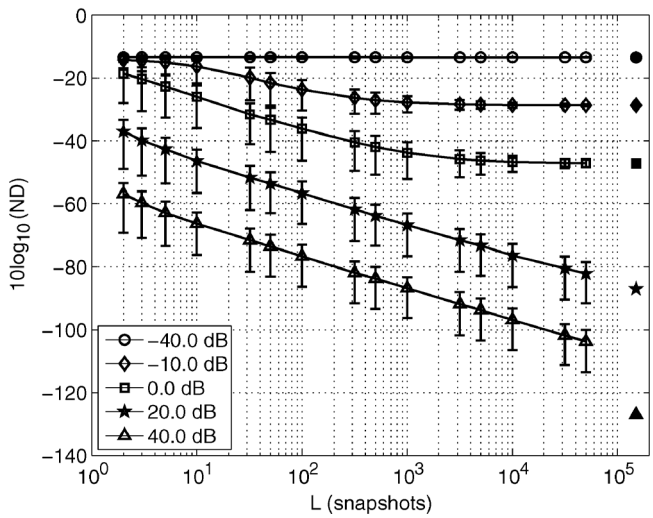

Fig. 8. DMR ND as a function of snapshots for the canonical example. Results are shown for five INR levels: −40, −10, 0, 20, and 40 dB. The symbols denote the mean ND and the error bars mark the span between the 10th and 90th percentiles of the data. The five filled symbols on the far right-hand side of the plot indicate the ND of the associated ensemble DMR beamformer.

side of the plot indicate the ensemble results for each of the INR levels. Fig. 8 highlights several important points about the snapshot dependence of the DMR ABF. For the lowest INR shown on the plot (−40 dB), the ND remains constant at the same value as the CBF. For INRs of −10 and 0 dB, ND decreases with snapshots until it reaches the ensemble value, where it levels off. At the higher INR values, ND decreases at a rate of 10 dB/decade of snapshots over the five-decade range shown on the plot. Extrapolating the 10-dB/decade slope for the higher INR cases predicts the number of snapshots required to reach the ensemble ND. The 20-dB case requires more than 10^5 snapshots, and the 40-dB case requires more than 10^6 snapshots. It is unrealistic to expect that these large numbers of snapshots will be available in any practical scenario.

The error bars in Figs. 7 and 8 indicate the variability of DMR ND around the mean. As the ND decreases, the error bars maintain approximately constant spread for INRs above 0 dB. Since a log scale is used in these figures, this implies that the variability decreases with increasing ND. Examining the standard deviation of ND shows that for high INR, the slope of the standard deviation versus INR curve is -1, i.e., a 10-dB decrease in standard deviation for every 10-dB increase in INR. Similarly, the standard deviation decreases 10 dB for every decade of snapshots for high INRs. This suggests that the standard deviation of DMR ND for high INR is $\mathcal{O}(1/(L \cdot \mathrm{INR}))$.

The main conclusions about ND derived from the canonical example are as follows. For INRs below a threshold, the DMR ABF does not "see" the interferer and the mean ND is equal to the CBF result. The INR threshold depends on the number of snapshots. Above the threshold, the mean ND decreases linearly when plotted on a log–log scale. The slope of the mean ND curves is predictable, suggesting that a piecewise linear model for ND could be constructed. The difference in the slope of ND versus INR curves explains why no snapshot implementation can attain the deep notches associated with the ensemble beamformer. The standard deviation of DMR ND is inversely proportional to INR and snapshots.

C. Effect of Interferer Location on Notch Depth

This section investigates the effect of the interferer location on DMR ND. The purpose is to assess whether the conclusions of the previous section are applicable in general. Fig. 9 shows the ND versus INR results for two different cases. Compared to the canonical example (Table I), the only difference in these cases is the interferer location u_1. In the first case, $u_1 = 0.0405$, which is a point near the first null of the CBF beampattern (see Fig. 1). Comparing Fig. 9(a) with Fig. 7 indicates that the ND for this alternate interferer case shares two important characteristics with the canonical example. First, for high INRs, the slopes of the lines in Fig. 9(a) are the same as in Fig. 7. For $L = 2$ and 100, the slope is -1. For $L = 50\,000$, the slope is initially -2 (following the ensemble prediction) and switches to -1 above a threshold INR. The INR threshold where the slope changes from -2 to -1 depends on the interferer location. The second common feature of Figs. 9(a) and 7 is that the error bars for high INRs indicate approximately constant spread. Log–log plots of the standard deviation versus INR show a slope of -1 for INRs above 0 dB in both the canonical example and the $u_1 = 0.0405$ case. This suggests that the spread of the ND around the mean is proportional to the mean, independent of interferer location. There are some noticeable differences in Figs. 9(a) and 7. While the mean ND starts near the CBF ND for the $u_1 = 0.0405$ case, it is not exactly equal to this value. Also, the ND associated with the alternate interferer goes up slightly before beginning its linear descent for the $L = 2$, 100 snapshot cases.

Fig. 9(b) shows ND as a function of INR for the case where the interferer is located exactly at the null of the CBF beampattern, i.e., $u_1 = 0.0400 = 2/N$. Note that the results for this case are almost identical to the $u_1 = 0.0405$ case. The only major difference is the shape of the $L = 50\,000$ results for INRs below 0 dB. For an interferer located at a null of the CBF, the ND of the sample DMR beamformer is far away from the ND of the CBF and the ensemble DMR ABF, both of which are exactly equal to zero on a linear scale ($-\infty$ on a log scale).

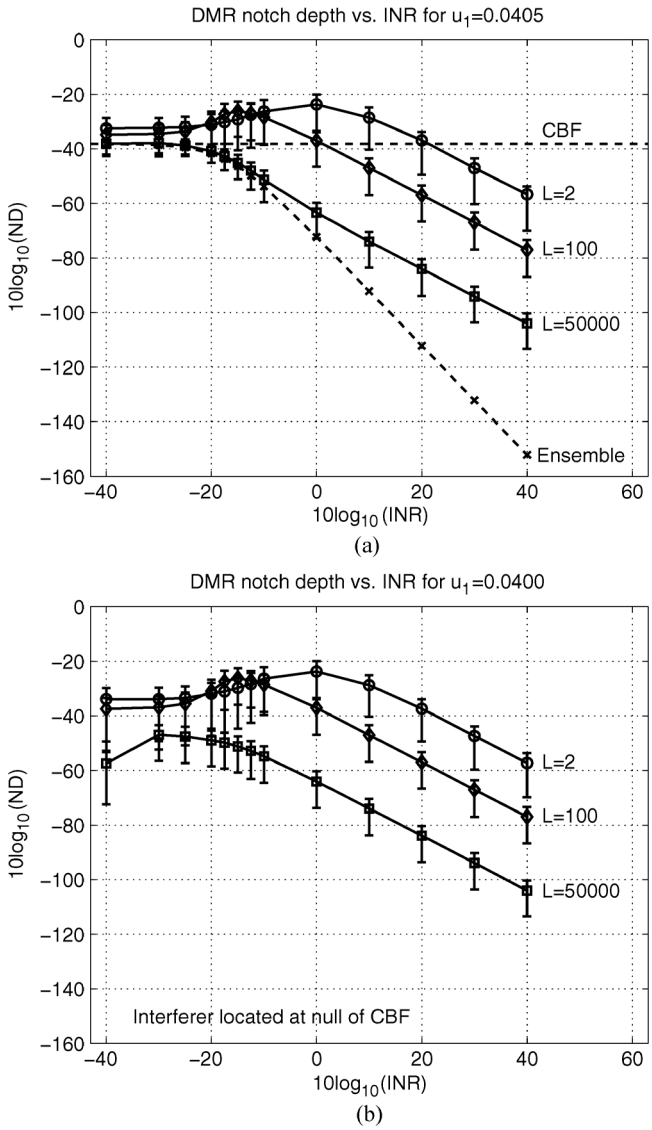

Fig. 9. DMR ND as a function of INR for two different interferer locations. Other than the interferer angle, all other simulation parameters are identical to the canonical single-interferer example (Table I). Results are shown for DMR ABFs generated using three different numbers of snapshots. The symbols denote the mean ND and the error bars mark the span between the 10th and 90th percentiles of the data. The CBF and ensemble DMR results are shown for the first case. For the second case, both the CBF and ensemble NDs are identically zero, which is off the scale of the decibel plot. (a) ND versus INR for interferer located near a null of conventional beampattern. (b) ND versus INR for interferer located at a null of conventional beampattern.

These examples demonstrate that the important conclusions about ND slope and variability derived from the canonical single-interferer example are valid for other interferer locations. The dependence of ND on u_1 is strongest for low INR. Finally, the example in Fig. 9(b) indicates that DMR does not maintain the nulls of the CBF when it is implemented using the SCM instead of the ECM.

D. White Noise Gain Statistics

This section analyzes the WNG of the DMR ABF as a function of INR and snapshots. Fig. 10 illustrates how WNG varies with INR for the canonical single-interferer example. The solid lines show the mean WNG for $L = 2$, 100, and 50 000 snapshots. The mean ND versus INR plots for these cases are very similar to the ensemble result shown in Fig. 3. Specifically, the mean WNG starts at a fixed level below $10\log_{10}(N)$ and rolls off as INR increases, eventually approaching $\mathrm{WNG}_{\mathrm{asympt}}$. The WNG for low INR is a function of the number of snapshots. For larger L values, WNG is closer to the optimal value. For 50 000 snapshots, WNG is essentially equal to the optimal value for INRs less than or equal to -30 dB. The INR at the rolloff point is also a function of L. For $L \geq N$, this point matches the ensemble result. For the snapshot-deficient case $(L = 2)$, the rolloff starts at a slightly higher INR.

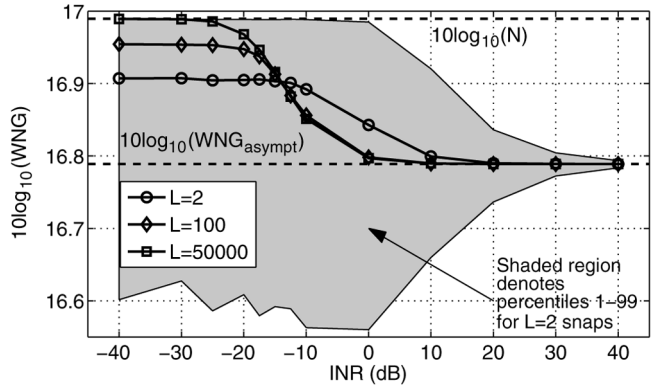

Fig. 10. Mean DMR WNG as a function of INR for the canonical example. Results are shown for ABFs generated using 2, 100, and 50 000 snapshots. The dashed lines indicate the optimal value of $10\log_{10}(N)$, which is the WNG of the CBF, and the asymptotic value $10\log_{10}(\mathrm{WNG}_{\mathrm{asympt}})$ derived in Section III-C.

Fig. 10 also illustrates the variability of the WNG. The shaded region in the plot indicates the 1st and 99th percentiles for the $L = 2$ case. The percentile lines for the $L = 100$ and 50 000 cases lie inside the shaded region. Note that the WNG variability is quite small. The 1st and 99th percentiles lie within 0.25 dB of $\mathrm{WNG}_{\mathrm{asympt}}$ and within 0.43 dB of the optimal value $10\log_{10}(N)$. For large INRs, WNG is concentrated around the asymptotic value $\mathrm{WNG}_{\mathrm{asympt}}$.

This section indicates that WNG of the DMR ABF has very low variability. This is true as long as the interferer is located away from the steering direction (outside the 3-dB points of the ML). As INR increases, the mean WNG converges to $\mathrm{WNG}_{\mathrm{asympt}}$. The narrowing of the shaded region around the asymptotic mean indicates that the distribution is highly concentrated for high INRs.

E. SINR Statistics

Recall that for the single-interferer example, SINR is simply the ratio of the SNR to the sum of the interferer and noise powers

$$\mathrm{SINR} = \frac{\mathrm{SNR}}{\mathrm{INR}\cdot\mathrm{ND} + 1/\mathrm{WNG}}. \tag{29}$$

Similar to the ensemble case, a plot of the interferer and noise components in the denominator of the SINR equation provides useful intuition. Fig. 11 compares the mean $\mathrm{INR}\cdot\mathrm{ND}$ for different numbers of snapshots to the mean 1/WNG. Results are shown on a log scale. For low INR, the interferer power for all snapshot cases is identical to the ensemble predictions shown in Fig. 4. As INR increases, the curves for the three snapshot cases

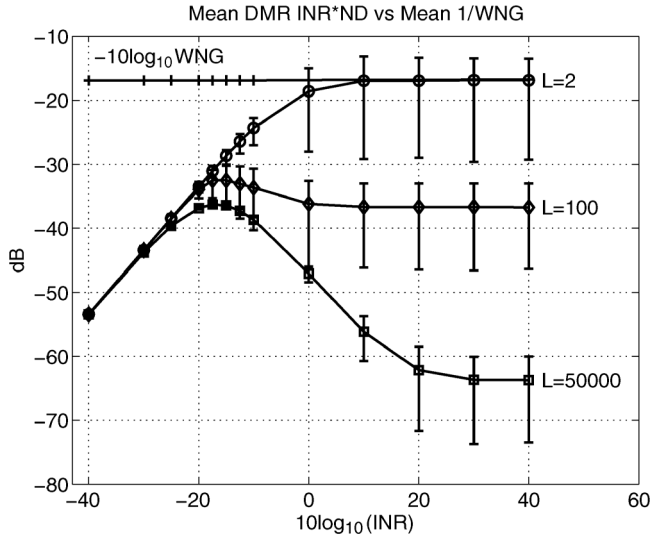

Fig. 11. Comparison of the mean interferer and white noise terms in the denominator of (29) for the canonical single-interferer example. Results are shown for three different numbers of snapshots: $L = 2$, 100, and 50 000.

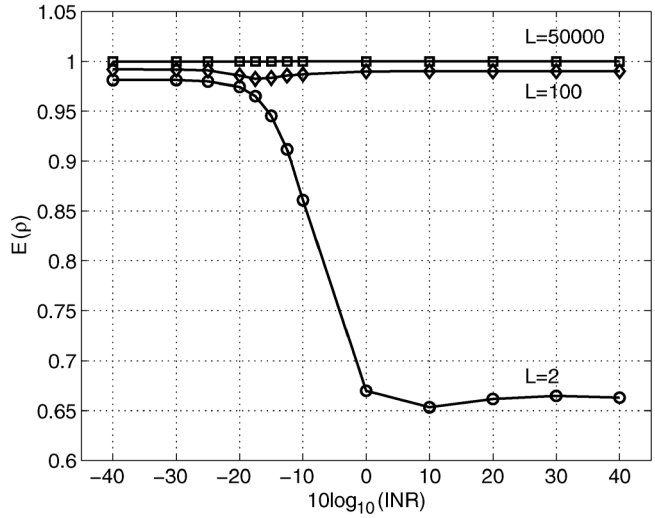

Fig. 12. Mean SINR loss for the DMR ABF as a function of INR for the canonical example. Results are shown for three different numbers of snapshots: $L = 2$, 100, and 50 000.

separate from one another. Unlike the ensemble result that decreases as INR gets large, INR · ND for the sample DMR ABF levels out at a fixed value that depends on L. This behavior makes sense in light of the ND versus INR results shown in Fig. 7. The slope of ND versus INR for sample DMR is -1 over most of its range, whereas it is -2 for ensemble DMR. These results indicate that once the INR is sufficiently high, the net effect of the interferer at the output of the DMR ABF is independent of the interferer power, and depends only on the number of snapshots. In essence, the beamformer is "treading water" with respect to the interferer. It is not falling behind (letting more of the interferer through), but it is not increasing its lead either (which ensemble DMR does by making its notch proportionately deeper).

As defined in Section II-A, the SINR loss ρ is the ratio of the SINR obtained with L snapshots to the ensemble SINR. Using the definition of SINR for the single-interferer example in (29) and the simplified result in (28) for SINR_{ens}, SINR loss is

$$\rho = \frac{\text{SINR}}{\text{SINR}_{\text{ens}}} = \frac{1}{\text{WNG}_{\text{ens}}} \cdot \frac{1}{\text{INR} \cdot \text{ND} + 1/\text{WNG}}. \qquad (30)$$

The above expression assumes the interferer is outside the ML. As shown in Fig. 3, WNG_{ens} is very close to N for all INRs. Thus, the first factor in (30) is a constant. This suggests that the behavior of the SINR loss for a single interferer depends only on the INR · ND and 1/WNG terms shown in Fig. 11. Given this intuition, consider what the mean SINR loss looks like for the canonical example. Fig. 12 shows how $\mathcal{E}\{\rho\}$ varies with INR for three snapshot cases: $L = 2$, 100, and 50 000. As expected from the discussion of the "treading water" phenomenon above, the mean SINR loss is essentially independent of the INR once INR reaches a snapshot-dependent threshold. For this 50-sensor case, the threshold INR is approximately 0 dB.

Fig. 13 shows the trend in the mean SINR loss as a function of the number of snapshots. The results are shown for four different INR values. Note that the mean for the 40-dB INR case is representative of the mean for INRs above 0 dB since the mean is independent of INR for these cases (as shown in Fig. 12).

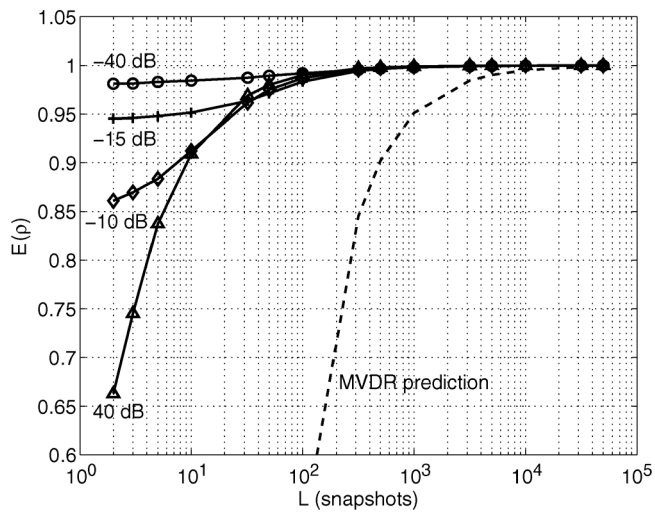

Fig. 13. Mean SINR loss for the DMR ABF as a function of snapshots for the canonical example. Results are shown for INRs between −40 and 40 dB. The dashed line shows the predicted mean SINR loss for the MVDR ABF, as derived by Reed *et al.* [2].

For reference, Fig. 13 shows the predicted mean SINR loss for the MVDR ABF derived by Reed *et al.* [2]. Note that this result is only valid for $L \geq N$ since the SCM used to compute the MVDR weights must be full rank. Reed *et al.* predict that the MVDR ABF requires twice as many snapshots as sensors to achieve $\mathcal{E}\{\rho\} = 0.5$, whereas Fig. 13 shows that DMR requires only two snapshots to achieve the same result. It is important to note that the analysis in [2] is not limited to the single-interferer case. The DMR result reported here is consistent with the claim for other eigenspace ABFs that two snapshots per interferer are required for $\mathcal{E}\{\rho\} \geq 0.5$. Section VII considers the relationship to other ABF results in more detail. Before that discussion, it is important to demonstrate that the sample eigenvectors control DMR performance and to relate these empirical results to RMT predictions. Section V examines the role of the eigenvectors, and Section VI describes the relevant RMT results.

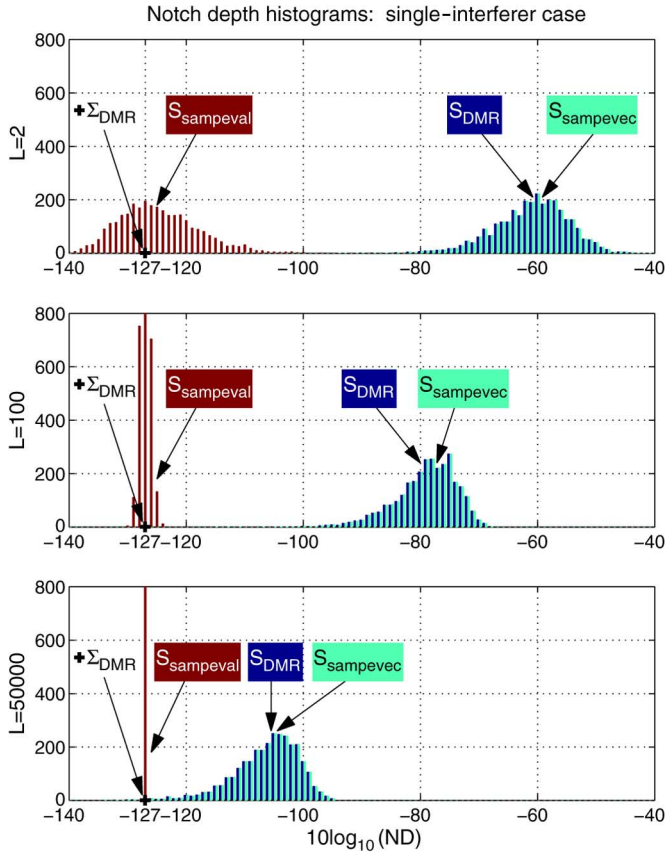

Fig. 14. Histograms of ND for the canonical example. The four panels show results for different numbers of snapshots: $L = 2$, 100, and 50 000. Each panel contains results for three beamformers generated using different structured covariance matrices: $\mathbf{S}_{\mathrm{DMR}}$ (blue), $\mathbf{S}_{\mathrm{sampevec}}$ (green), $\mathbf{S}_{\mathrm{sampeval}}$ (red), and $\mathbf{\Sigma}_{\mathrm{DMR}}$ (black cross). The $\mathbf{S}_{\mathrm{DMR}}$ and $\mathbf{S}_{\mathrm{sampevec}}$ histograms are indistinguishable.

V. Eigenvalues Versus Eigenvectors

The DMR weight vector depends on the eigendecomposition of the SCM. This section investigates the relative influence of the sample eigenvalues and eigenvectors on ND. Fig. 14 compares the standard DMR ABF (generated with sample statistics) with two alternative DMR implementations. The first of these alternative beamformers uses the ensemble eigenvectors and the sample eigenvalues to generate the structured covariance $\mathbf{S}_{\mathrm{sampeval}}$ used in its weight vector

$$\mathbf{S}_{\mathrm{sampeval}} = \sum_{n=1}^{D} g_n \boldsymbol{\xi}_n \boldsymbol{\xi}_n^{\mathrm{H}} + \sum_{n=D+1}^{N} s_w^2 \boldsymbol{\xi}_n \boldsymbol{\xi}_n^{\mathrm{H}}. \qquad (31)$$

The second uses the ensemble eigenvalues and the sample eigenvectors to generate the structured covariance $\mathbf{S}_{\mathrm{sampevec}}$ used in its weight vector

$$\mathbf{S}_{\mathrm{sampevec}} = \sum_{n=1}^{D} \gamma_n \mathbf{e}_n \mathbf{e}_n^{\mathrm{H}} + \sum_{n=D+1}^{N} \sigma_w^2 \mathbf{e}_n \mathbf{e}_n^{\mathrm{H}}. \qquad (32)$$

While these alternative formulations cannot be implemented in practice, employing them in a simulation environment can answer the question of whether the eigenvalues or eigenvectors control DMR performance.

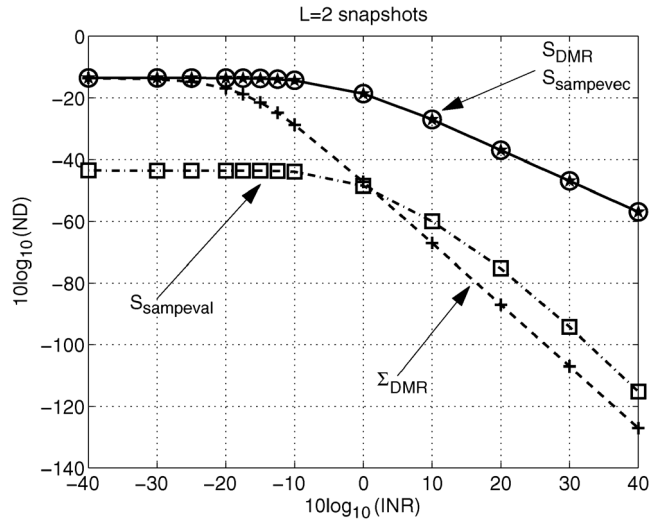

Fig. 15. Mean ND as a function of INR for four beamformers constructed with four covariance matrices: $\mathbf{S}_{\mathrm{DMR}}$ (stars), $\mathbf{S}_{\mathrm{sampeval}}$ (circles), $\mathbf{S}_{\mathrm{sampevec}}$ (squares), and $\mathbf{\Sigma}_{\mathrm{DMR}}$ (crosses). Results are shown for the $L = 2$ snapshot case.

Fig. 14 shows histograms of ND for the canonical single-interferer example considered previously. The INR is 40 dB, and the histograms contain data from 3000 Monte Carlo trials. The three panels show the results for different numbers of snapshots: 2, 100, and 50 000. Each panel shows histograms of ND for the standard DMR ABF and the two alternative beamformers. Black crosses indicate the ensemble ND (-127 dB in all cases). When the ensemble eigenvectors are used to construct the covariance matrix $\mathbf{S}_{\mathrm{sampeval}}$, the resulting histogram is centered on the ensemble ND. In contrast, when the sample eigenvectors are used to construct the covariance matrix $\mathbf{S}_{\mathrm{sampevec}}$, the histogram is centered on the standard DMR result. The sample eigenvector results are indistinguishable from the standard DMR results in this plot. Fig. 14 demonstrates that the accuracy of the sample eigenvectors determines how well the DMR ABF can eliminate a loud interferer.

Fig. 15 shows that the sample eigenvectors control ND regardless of INR. The plot displays the mean ND as a function of INR for the four beamformers: standard DMR, DMR with sample eigenvalues, DMR with sample eigenvectors, and ensemble DMR. Results are shown for the two-snapshot case. Over the entire range of INRs shown (from -40 to $+40$ dB), the mean ND of the alternative sample eigenvector beamformer lies on top of the standard DMR result. For INRs greater than 0 dB, the alternative sample eigenvalue beamformer follows the same trend as the ensemble DMR beamformer. For INRs less than 0 dB, the sample eigenvalue beamformer has a lower ND than the ensemble beamformer. As L increases, the sample eigenvalue beamformer rapidly converges to the ensemble result.

The simulations in this section demonstrate that the sample eigenvectors determine the ND of the DMR ABF. Since ND is fundamentally related to SINR, it follows that predicting the overall performance of the DMR beamformer requires an understanding of the behavior of the sample eigenvectors. Section VI reviews recent RMT results that characterize the accuracy of the sample eigenvectors.

VI. Insights From RMT

As noted in the introduction, recent work on RMT contains valuable insights about the behavior of the eigenvalues and eigenvectors of large random matrices. The book by Bai and Silverstein provides a comprehensive overview of the mathematical results in this area [17]. Since the SCM is a random matrix, RMT is applicable to analyze adaptive beamforming problems. For example, Richmond *et al.* [24] use RMT to study the behavior of diagonally loaded MVDR ABFs. Nadakuditi's dissertation is a major contribution to the application of RMT to array processing [25]. In addition to discussing the MVDR results, the dissertation describes a new rank estimator for signals in white noise. The rank estimator uses RMT predictions of the sample eigenvalues along with the Akaike information criterion. See the subsequent journal article by Nadakuditi and Edelman [26] for more information.

As shown in Section V, the sample eigenvectors have a greater impact on DMR performance than the sample eigenvalues. Several authors have RMT results on the fidelity of eigenvectors that are relevant to the analysis of the DMR ABF. Paul [18], Nadler [19], Johnstone and Lu [20], and Benaych-Georges and Nadakuditi [21] describe the eigenvectors of the *spiked covariance model*. This model assumes that the data consist of one or more loud signals plus white noise. The RMT analysis of the spiked covariance case is asymptotic: $N, L \to \infty$ and the ratio $N/L \to c$. Unlike traditional asymptotic analyses of ABFs (N fixed, $L \to \infty$), RMT provides useful predictions for snapshot-deficient cases ($c > 1$). The key result related to DMR is a prediction of the limiting value of the generalized cosine between the ensemble eigenvector and the sample eigenvector

$$\cos^2(\boldsymbol{\xi}_i, \mathbf{e}_i) \xrightarrow{\text{a.s.}} \begin{cases} 0, & \text{if } N\dfrac{\sigma_i^2}{\sigma_w^2} \le \sqrt{c} \\ \dfrac{1 - c\left(\dfrac{\sigma_w^2}{N\sigma_i^2}\right)^2}{1 + c\dfrac{\sigma_w^2}{N\sigma_i^2}}, & \text{if } N\dfrac{\sigma_i^2}{\sigma_w^2} > \sqrt{c}. \end{cases} \tag{33}$$

Note that $N\sigma_w^2/\sigma_1^2 = N \cdot \text{INR}$ is the output SNR that would be associated with a CBF steered toward the exact interferer direction. Equation (33) describes a *phase transition phenomenon*. When $N \cdot \text{INR}$ is below the $\sqrt{c}$ threshold, $\mathbf{e}_i$ is orthogonal to $\boldsymbol{\xi}_i$. When $N \cdot \text{INR}$ is above this threshold, $\mathbf{e}_i$ is a biased estimate of $\boldsymbol{\xi}_i$. The threshold is the square root of the ratio of sensors to snapshots. Fig. 16 shows how the $\cos^2$ prediction varies with INR and L for a 50-sensor array.

The phase transition behavior of the sample eigenvectors explains several important aspects of DMR performance. First, it explains why DMR ND is equal to the CBF ND for low INR. For interferers below the threshold, the sample eigenvector is orthogonal to the true eigenvector, meaning that the beamformer knows nothing about the location of the interferer. For a 50-sensor array operating with a single snapshot, the threshold is exceeded by interferers with INRs of -8.5 dB and higher. As the array accumulates more snapshots, the threshold decreases, meaning that the array can "see" interferers with even lower INRs. Fig. 16 illustrates the change in threshold as a function of snapshots.

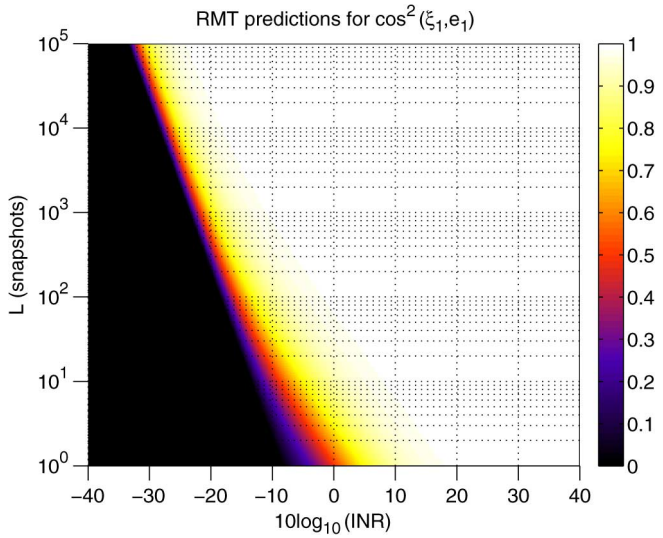

Fig. 16. RMT predictions of the generalized cosine squared between the ensemble eigenvector and the sample eigenvector as a function of INR and snapshots. Results are shown for a 50-sensor array.

Second, the phase transition described in (33) explains why the DMR ABF fails to achieve the ensemble ND in many cases. When the interferer exceeds the threshold, the sample eigenvectors are biased since $\cos^2(\boldsymbol{\xi}_i, \mathbf{e}_i) \neq 1$ for any value of $c > 0$. The bias vanishes as $c \to 0$, and the rate at which it vanishes depends on the INR. This agrees with the DMR ND versus snapshot results shown in Fig. 8. ND decreases as L increases. Since the array size is fixed ($N = 50$), an increase in L means a decrease in c. Fig. 8 also shows that the number of snapshots required to achieve ensemble performance is a function of INR.

Before the development of the RMT results discussed above, most analyses of the sample eigenvectors relied on perturbation theory [27]–[29]. The perturbation approximation is $\mathcal{O}(L^{-1})$, thus it is applicable for high numbers of snapshots. Cox conjectured an approximate expression for the generalized sine squared between the ensemble and sample eigenvectors [30] that yields reasonable results for lower numbers of snapshots

$$\sin^2(\boldsymbol{\xi}_i, \mathbf{e}_i) \approx \frac{1}{\text{INR}\left(L - \dfrac{1}{L}\right)}. \tag{34}$$

Using (33) the corresponding RMT result for a component above the threshold is

$$\sin^2(\boldsymbol{\xi}_i, \mathbf{e}_i) = \frac{N \cdot \text{INR} + 1}{NL \cdot \text{INR}^2 + N \cdot \text{INR}}. \tag{35}$$

In the limit of large INR, both predictions for $\sin^2$ reduce to $1/(L \cdot \text{INR})$.

VII. Relationship to Other ABF Results

Sections IV and V investigated the performance of the DMR ABF when the weights are estimated using sample statistics.

The purpose of this section is to discuss how these DMR results relate to prior work on ABFs. While there are no analytical predictions for DMR performance as a function of snapshots, such results exist for other algorithms.

Reed *et al.*'s seminal work [2] on MVDR performance predicts the expected value of SINR loss as a function of the array size and snapshots

$$\rho_{\mathrm{MVDR}} = \frac{L+2-N}{L+1}. \tag{36}$$

Note that this result is valid for $L \geq N$ because the MVDR weight vector can only be computed when the covariance matrix is full rank. Fig. 13 compares the SINR loss for the DMR ABF to the MVDR prediction. For the single-interferer example, the DMR ABF converges to the optimal SINR significantly faster than the MVDR ABF. This is a well-known advantage of eigenspace methods [4, pp. 845–850].

As indicated in Section I, Chang and Yeh [6] and Feldman and Griffiths [7] analyzed the performance of a different type of eigenspace ABF than DMR. Their algorithm operates on the signal-plus-noise subspace, whereas DMR uses only the noise subspace. They show that the SINR for the eigenspace ABF implemented with the SCM depends on both the subspace dimension and the SINR for the ensemble case. In general, the louder the signal component, the greater the number of snapshots required to achieve adequate performance. The results of [6] and [7] are not directly applicable to DMR because the DMR ABF excludes eigenvectors associated with the signal from its dominant subspace. It is important to note that these derivations for the eigenspace ABF assume that $L \geq N$, similar to [2]

Much of the prior work on ABF performance focuses on SINR rather than on the beampattern, thus there are few results to compare with the DMR ND analysis presented in this paper. Richmond's work on the MVDR ABF is the most relevant [31]. He derives the probability density function (pdf) and cumulative distribution function (cdf) of the magnitude response and computes the probability that a sidelobe is below a given threshold. A detailed comparison of the DMR results and Richmond's MVDR predictions is beyond the scope of this paper. It is important to note that the derivation in [31] also assumes $L \geq N$, thus it does not address the snapshot-deficient case.

The discussion above highlights the lack of ABF results for cases where $L < N$. Based on Section VI, RMT offers great promise for analyzing the snapshot-deficient scenarios that are of great practical interest. Section VIII summarizes the paper and comments on some possible directions for further research.

VIII. Conclusion

This paper presents a theoretical analysis and an empirical study of the DMR ABF for the single-interferer example. The theoretical calculations for the ensemble case provide valuable insights into the relationship among notch depth, white noise gain, and SINR. The important results for the ensemble case are that the loss in WNG due to placing a notch only depends on the location of the notch and that the ensemble ND is guaranteed to be deep enough so that the SINR depends only on the white noise component.

The empirical study reveals several key points. First, the snapshot performance of the DMR ABF primarily depends on the sample eigenvectors. The sample eigenvalues have very little effect. Second, DMR performance metrics have a phase transition that is similar to the one predicted by RMT for the sample eigenvectors. The INR associated with the phase transition is a function of the size of the array and the number of snapshots. Third, above the transition, the mean ND on a log–log scale has a predictable slope as a function of snapshots and INR. The standard deviation of ND also follows a linear trend. These results suggest that a piecewise linear model for DMR ND is appropriate. Fourth, for interferers outside the ML associated with the steering direction, WNG is concentrated around the ensemble prediction and is close to the optimal value. Finally, for a single interferer, the mean SINR is within 3 dB of optimal for two snapshots or more, consistent with the claim of other eigenspace ABFs that two snapshots per interferer are required for $\mathcal{E}\{\rho\} \geq 0.5$.

The results presented in this paper suggest several possibilities for further research. The evidence of the phase transition in the ND results indicates that the RMT predictions for the sample eigenvectors are useful for constructing a model of DMR ND. Such a model would provide valuable information for sonar performance predictions. A recent conference paper describes our work on an analytical model of the mean DMR ND based on RMT [32]. A companion paper compares the RMT model predictions to experimental measurements [33]. The latter publication considers the problem of two interferers, but additional research needs to be done on how DMR handles multiple interferers. An important aspect of the multiple-interferer case is the rank estimation problem, which has not been addressed in the single-interferer examples examined here. In addition to rank estimation, mismatch is another important topic that future work should address. A mismatch analysis of the DMR ABF, similar to Gilbert and Morgan's work [34] on MVDR, would be very valuable.

Acknowledgment

The authors would like to thank D. Abraham, A. Baggeroer, H. Cox, K. Davidson, S. Kraut, R. Rao Nadakuditi, C. Richmond, and J. Tague for helpful discussions. They would also like to thank the anonymous reviewers for their constructive comments on the manuscript.

References

[1] J. Capon, "High-resolution frequency-wavenumber spectrum analysis," *Proc. IEEE*, vol. 57, no. 8, pp. 1408–1418, Aug. 1969.

[2] I. Reed, J. Mallett, and L. Brennan, "Rapid convergence rate in adaptive arrays," *IEEE Trans. Aerosp. Electron. Syst.*, vol. AES-10, no. 6, pp. 853–863, Nov. 1974.

[3] R. A. Monzingo and T. W. Miller, *Introduction to Adaptive Arrays*. Raleigh, NC, USA: SciTech, 2004, pp. 293–300.

[4] H. L. Van Trees, *Optimum Array Processing*. New York, NY, USA: Wiley, 2002.

[5] E. K. L. Hung and R. M. Turner, "A fast beamforming algorithm for large arrays," *IEEE Trans. Aerosp. Electron. Syst.*, vol. AES-19, no. 4, pp. 598–607, Jul. 1983.

[6] L. Chang and C.-C. Yeh, "Performance of DMI and eigenspace-based beamformers," *IEEE Trans. Antennas Propag.*, vol. 40, no. 11, pp. 1336–1347, Nov. 1992.

[7] D. D. Feldman and L. J. Griffiths, "A projection approach for robust adaptive beamforming," *IEEE Trans. Signal Process.*, vol. 42, no. 4, pp. 867–876, Apr. 1994.
[8] D. A. Abraham and N. L. Owsley, "Beamforming with dominant mode rejection," in *Proc. IEEE OCEANS Conf.*, 1990, pp. 470–475.
[9] H. Cox and R. Pitre, "Robust DMR and multi-rate adaptive beamforming," in *Proc. 32nd Asilomar Conf. Signals Syst. Comput.*, 1998, pp. 920–924.
[10] H. Cox, R. Pitre, and H. Lai, "Robust adaptive matched field processing," in *Proc. 32nd Asilomar Conf. Signals Syst. Comput.*, 1998, pp. 127–131.
[11] S. M. Kogon, "Robust adaptive beamforming for passive sonar using eigenvector/beam association and excision," in *Proc. IEEE Sensor Array Multichannel Signal Process. Workshop*, 2002, pp. 33–37.
[12] C. Bao, "Robust high resolution dominant mode rejection (DMR) beamformer for passive sonar," in *Proc. ACOUSTICS Gold Coast, Australia: Austral. Acoust. Soc.*, 2004, pp. 523–526.
[13] N. Li, J. Tang, Y. Peng, and X. Wang, "An improved dominant mode rejection adaptive beamforming algorithm," in *Proc. CIE Int. Conf. Radar*, Oct. 2006, DOI: 10.1109/ICR.2006.343294.
[14] S. M. Kogon, "Experimental results for passive sonar arrays with eigenvector-based adaptive beamformers," in *Proc. 36th Asilomar Conf. Signals Syst. Comput.*, 2002, vol. 1, pp. 439–447.
[15] T. R. Messerschmitt and R. A. Gramann, "Evaluation of the dominant mode rejection beamformer using reduced integration times," *IEEE J. Ocean. Eng.*, vol. 22, no. 2, pp. 385–392, Apr. 1997.
[16] T. M. Redheendran and R. A. Gramann, "Initial evaluation of the dominant mode rejection beamformer," *J. Acoust. Soc. Amer.*, vol. 104, no. 3, pp. 1331–1344, Sep. 1998.
[17] Z. Bai and J. W. Silverstein, *Spectral Analysis of Large Dimensional Random Matrices*, 2nd ed. New York, NY, USA: Springer-Verlag, 2010.
[18] D. Paul, "Asymptotics of sample eigenstructure for a large dimensional spiked covariance model," *Statistica Sinica*, vol. 17, pp. 1617–1642, 2007.
[19] B. Nadler, "Finite sample approximation results for principal component analysis: A matrix perturbation approach," *Ann. Stat.*, vol. 36, no. 6, pp. 2791–2817, 2008.
[20] I. M. Johnstone and A. Y. Lu, "On consistency and sparsity for principal components analysis in high dimensions," *J. Amer. Stat. Assoc.*, vol. 104, no. 486, pp. 682–693, 2009.
[21] F. Benaych-Georges and R. R. Nadakuditi, "The singular values and vectors of low rank perturbations of large rectangular random matrices," *Adv. Math.*, vol. 227, no. 1, pp. 494–521, 2011.
[22] H. Cox, "Resolving power and sensitivity to mismatch of optimum array processors," *J. Acoust. Soc. Amer.*, vol. 54, no. 3, pp. 771–785, 1973.
[23] C. W. Therrien, *Discrete Random Signals and Statistical Signal Processing*. Englewood Cliffs, NJ, USA: Prentice-Hall, 1992.
[24] C. D. Richmond, R. R. Nadakuditi, and A. Edelman, "Asymptotic mean squared error performance of diagonally loaded Capon-MVDR processor," in *Proc. 39th Asilomar Conf. Signals Syst. Comput.*, Nov. 2005, pp. 1711–1716.
[25] R. R. Nadakuditi, "Applied stochastic eigenanalysis," Ph.D. dissertation, Massachusetts Inst. Technol./Woods Hole Oceanogr. Inst., Cambridge/Woods Hole, MA, USA, 2007.
[26] R. R. Nadakuditi and A. Edelman, "Sample eigenvalue based detection of high-dimensional signals in white noise using relatively few samples," *IEEE Trans. Signal Process.*, vol. 56, no. 7, pp. 2625–2638, Jul. 2008.
[27] M. Kaveh and H. Wang, "Threshold properties of narrow-band-signal-subspace array processing methods," in *Advances in Spectrum Analysis and Array Processing*, S. Haykin, Ed. Englewood Cliffs, NJ, USA: Prentice-Hall, 1991, vol. II, ch. 5, pp. 173–220.
[28] B. Friedlander, "On the statistics of eigenvectors of sample covariance matrices," in *Proc. 31st Asilomar Conf. Signals Syst. Comput.*, Nov. 1997, pp. 1297–1301.
[29] B. Friedlander and A. J. Weiss, "On the second-order statistics of the eigenvectors of sample covariance matrices," *IEEE Trans. Signal Process.*, vol. 46, no. 11, pp. 3136–3139, Nov. 1998.
[30] H. Cox, "Multi-rate adaptive beamforming (MRABF)," in *Proc. IEEE Sensor Array Multichannel Signal Process. Workshop*, 2000, pp. 306–309.
[31] C. D. Richmond, "MVDR adaptive sidelobes: Extending Ruze's formula and providing an exact calculation of the probability of sidelobe suppression," in *Proc. IEEE Sensor Array Multichannel Signal Process. Workshop*, Mar. 2000, pp. 73–76.
[32] J. R. Buck and K. E. Wage, "A random matrix theory model for the dominant mode rejection beamformer notch depth," in *Proc. IEEE Stat. Signal Process. Workshop*, Aug. 2012, pp. 824–827.
[33] K. E. Wage, J. R. Buck, M. A. Dzieciuch, and P. F. Worcester, "Experimental validation of a random matrix theory model for dominant mode rejection beamformer notch depth," in *Proc. IEEE Stat. Signal Process. Workshop*, Aug. 2012, pp. 820–823.
[34] E. N. Gilbert and S. P. Morgan, "Optimum design of directive antenna arrays subject to random variations," *Bell Syst. Tech. J.*, vol. 34, pp. 637–663, May 1955.

Kathleen E. Wage (S'88–M'00) received the B.S. degree in electrical engineering from the University of Tennessee, Knoxville, TN, USA, in 1990 and the S.M., E.E., and Ph.D. degrees from the Massachusetts Institute of Technology/Woods Hole Oceanographic Institution Joint Program, Cambridge/Woods Hole, MA, USA, in 1994, 1996, and 2000, respectively.

She is currently an Associate Professor at the Electrical and Computer Engineering Department, George Mason University, Fairfax, VA, USA. Her research interests include array processing, random matrix theory, underwater acoustics, and signal processing education.

Dr. Wage is a member of the American Geophysical Union, the Acoustical Society of America, the American Society of Engineering Education, Tau Beta Pi, Eta Kappa Nu, and Sigma Xi. She received the IEEE Mac Van Valkenburg Early Career Teaching Award (2008), the U.S. Office of Naval Research (ONR) Young Investigator Award (2005), and the ONR Ocean Acoustics Entry-Level Faculty Award (2002). She is an Associate Editor for the IEEE JOURNAL OF OCEANIC ENGINEERING and Chair of the IEEE Underwater Acoustic Signal Processing Workshop.

John R. Buck (S'90–M'96) received the S.B. degrees in electrical engineering and humanities (English literature) from the Massachusetts Institute of Technology (MIT), Cambridge, MA, USA, in 1989, and subsequently received the S.M., E.E., and Ph.D. degrees in electrical and ocean engineering from the MIT/Woods Hole Oceanographic Institution Joint Program, Cambridge/Woods Hole, MA, USA, in 1991, 1992, and 1996, respectively.

In 1996, he joined the faculty of the University of Massachusetts Dartmouth, North Dartmouth, MA, USA, where he is a Professor in the Department of Electrical and Computer Engineering. His research interests include signal processing, underwater acoustics, information theory, animal bioacoustics, and engineering pedagogy.

Dr. Buck is a member of the Acoustical Society of America, the American Society for Engineering Education, and Sigma Xi. His awards include the UMass Dartmouth Faculty Federation Leo M. Sullivan Teacher of the Year Award (2008), the IEEE Education Society Mac Van Valkenburg Early Career Teaching Award (2005), a Fulbright Senior Scholar Fellowship to Australia (2003), the U.S. Office of Naval Research (ONR) Young Investigator Award (2000), the National Science Foundation (NSF) CAREER award (1998) and the MIT Goodwin Medal (1994). He served as an Associate Editor for the IEEE JOURNAL OF OCEANIC ENGINEERING from 2005 to 2010, and thrice chaired the IEEE Underwater Acoustic Signal Processing Workshop.